IOP Publishing Plasma Sources Science and Technology
Plasma Sources Sci. Technol. **31** (2022) 095004 (15pp) https://doi.org/10.1088/1361-6595/ac882e

Parametric studies of stream instability-induced higher harmonics in plasma ionization breakdown near an emissive dielectric surface

De-Qi Wen[1,2,*], Peng Zhang[1], Janez Krek[2], Fu Yangyang[3] and John P Verboncoeur[1,2]

[1] Department of Electrical and Computer Engineering, Michigan State University, East Lansing, MI 48824, United States of America
[2] Department of Computational Mathematics, Science and Engineering, Michigan State University, East Lansing, MI 48824, United States of America
[3] Department of Electrical Engineering, Tsinghua University, Beijing 100084, People's Republic of China

E-mail: wendeqi@msu.edu

Received 27 September 2021, revised 25 July 2022
Accepted for publication 9 August 2022
Published 7 September 2022

Abstract

In this work, we comprehensively investigate the generation of higher harmonic (HH) electric fields normal to the applied rf electric field in multipactor-coexisting plasma breakdown by fully kinetic particle-in-cell (PIC) simulations and a theoretical model. Firstly, a base case at driving frequency 1 GHz, transverse rf electric field amplitude 3 MV m^{-1}, and background gas pressure 0.2 Torr, is studied in detail. The enhanced harmonic frequency observed is around ten times the fundamental rf frequency, significantly lower than the Langmuir frequency. A theoretical model reveals that the fundamental mechanism of HHs generation is stream–plasma instability, which originates from stream-like secondary electron emission interacting with plasma. The resulting HH frequency and the growth rate of its oscillating amplitude from the theoretical model, agree well with the PIC simulations. With increasing pressure, the HH oscillations are found to be significantly reduced. This is because at higher pressure the gas ionization rate is higher, which causes a more rapidly increasing plasma density, leaving less time for the growth of instability. Furthermore, the parameter space in terms of background gas pressure and rf field amplitude within which the HHs appear is revealed. Finally, the effect of the driving rf frequency on HHs is also investigated, and it is found that the instability-induced oscillating HHs field remains when the driving frequency is increased to 2 GHz, however, it is highly reduced at higher driving frequency of 5 GHz, as oscillations at the fundamental frequency start playing a more important role.

Keywords: electron dynamics, plasma–surface interaction, stream–plasma instability, plasma ionization breakdown, higher harmonics, multipactor discharge, particle-in-cell simulation and theory

(Some figures may appear in colour only in the online journal)

* Author to whom any correspondence should be addressed.

1. Introduction

High power microwave (HPM) systems are widely applied in many fields, such as space-based satellite communication, cyclotron heating in fusion energy, low temperature plasma material processing, as well as rf accelerators [1–10]. With increasing microwave power, a multipactor and plasma discharge near the microwave window can be easily triggered, and negatively affects power transmission. Meanwhile, the multipactor accompanied by intense secondary electron emission is also an important subject relevant to plasma surface interaction. Therefore, the relevant studies have attracted substantial research efforts in recent years.

The vacuum discharge is dominated by the multipacting process, where electrons gain energy from the rf electric field and impact the dielectric surface to induce a secondary electron yield (SEY) above unity [2, 5, 6, 8]. The residual positive charge on the dielectric surface produces a normal electric field, pointing away from the surface, which attracts the primary electrons back to the surface to eject more electrons. This process repeats until the time averaged SEY equals to unity, namely, a saturation state. For such a kind of multipactor discharge, Kishek and Lau [2] established susceptibility diagrams, in terms of the applied rf and restoring electric fields by analytical theory and single-particle Monte Carlo simulation [7, 11, 12]. Susceptibility diagrams allow estimation of the rf power over which multipactor would occur. Meanwhile, the multipactor saturation state is determined by the normal electric field due to surface charging and resulting impact energy distortion [13]. Later, full particle-in-cell (PIC) simulations found that the number of electrons oscillates at twice the driving frequency in the saturation state, and the trajectory of the rf field and surface normal field traces a Lissajous curve on the susceptibility curve [14]. To increase the breakdown threshold for a rf window, possible mitigations of multipactor have also been extensively explored [15–20], such as shaping the rf window structure, furnishing an external magnetic field, and tailoring the microwave signal.

When background gas or adsorbed gas from the rf window is present in space due to electron bombardment heating, multipactor dynamics significantly alters through collisions between electrons and neutrals [21]. Near atmospheric pressure, the secondary electrons from surface lose significant energy in flight through collisions, and the reduced impact energy suppresses the multipacting process on the dielectric surface over time [22]. Thus, electron–neutral collisions and plasma transport dominate the breakdown process in this case [4, 23–25]. In addition, in nanosecond high-power microwave discharges, it is experimentally found that plasma develops more intensively at the dielectric–air interface than in the free-space region [20], and the plasma propagates away from the surface. The propagation speed of plasma is further explained by photoionization at atmospheric pressure via PIC simulation under a spatially uniform transverse rf electric field [26].

In the pressure range from hundreds of mTorr to a few Torr, multipactor discharge and plasma ionization breakdown can coexist [22]. The scaling laws for the discharge formation time at various pressures were studied theoretically [27], and kinetically [22] for plasma discharges near rf window of HPM systems. It is well known that the HPM systems have important applications in space-based communication satellites, and multipactor/plasma discharges near the rf window has been a limiting factor for signal transmission, especially for the next generation communication satellites under design internationally requiring higher transmission power, where multipactor/plasma discharge is more easily triggered. Although the breakdown characteristics like plasma density at discrete moments were explored in the literature [22], the detailed time and space-dependent transient physics within one rf period during breakdown processes were barely investigated kinetically [28]. However, understanding the transient physics is essential for physicists and rf engineers to control and optimize the multipactor/plasma breakdown processes. We have three motivations in this work. Firstly, we provide a comprehensive and detailed understanding into the transient physics of multipactor/plasma breakdown near an rf window. Secondly, we investigated in more detail the physics of the enhanced higher harmonic (HH) components of the normal electric fields that in our short letter [29], especially its dependence on external conditions, which is important to the fundamental plasma physics during multipactor/plasma breakdown. Thirdly, in real world, signal distortion in space-based satellite communication can exist [30], and understanding the additional field components from multipactor/plasma discharge is an important subject, the HHs in the early stage of multipactor-induced plasma breakdown investigated here also provide potential insights into it.

In this work, we will present the detailed physics on HHs generation [29] in the early stage of plasma ionization breakdown at intermediate pressure (hundreds of mTorr) and the effect of the gas pressure and driving frequency on the discharge breakdown characteristics. The HH frequency spectrum is significantly enhanced at the frequency around ten times the rf frequency of 1 GHz, but much lower than the electron plasma frequency. It is significantly different from the harmonics for vacuum multipactor discharge in the previous works [11, 31]. Fully kinetic PIC simulations and theory studies are carried out. It is worth noting that the phenomenon of HHs is observed for argon, helium, as well as xenon, where gas species (characterized by collision reactions and cross section) are found to affect the parameter range, within which the HHs can be observed, but play a less important role in the phenomenon. Here we focus on argon discharges.

The paper is structured as follows: in section 2, we provide a description of our simulation including breakdown process, where the electron and ion–neutral collisions are introduced. The results and discussion are mainly presented in section 3. In subsection 3.1, the transient physics and HH generation for the base case with driving frequency $f = 1$ GHz, intermediate gas pressure $p = 0.2$ Torr, and transverse electric field amplitude $E_{\mathrm{rf0}} = 3$ MV m^{-1} [29], are discussed in detail

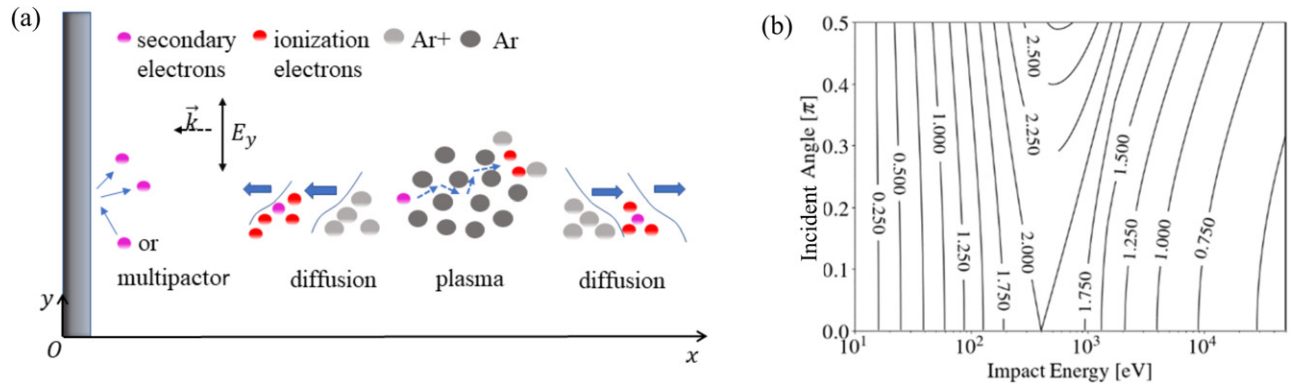

Figure 1. (a) Schematic of the multipactor and plasma discharge in kinetic PIC simulations; (b) the SEY as a function of the incident angle and impact energy of electrons in Vaughan's empirical formula [33].

Table 1. List of elementary processes included for argon. The references for the respective cross sections are provided in the right column.

	Reaction	Process (threshold)	Reference
1	$e^- + Ar \rightarrow e^- + Ar$	Elastic scattering	[38]
2	$e^- + Ar \rightarrow e^- + Ar^m$	Metastable excitation [11.55 (eV)]	[39]
3	$e^- + Ar \rightarrow e^- + Ar^r$	Resonant excitation [11.62 (eV)]	[39]
4	$e^- + Ar \rightarrow e^- + Ar^{4p}$	Excitation collision [13.2 (eV)]	[40]
5	$e^- + Ar \rightarrow e^- + Ar^{II}$	Group II excitation [14.09 (eV)]	[40]
6	$e^- + Ar \rightarrow e^- + Ar^{III}$	Group III excitation [14.71 (eV)]	[40]
7	$e^- + Ar \rightarrow e^- + Ar^h$	Highest excited states [15.20 (eV)]	[39]
8	$e^- + Ar \rightarrow 2e^- + Ar^+$	Impact ionization [15.76 (eV)]	[41, 42]
9	$Ar^+ + Ar \rightarrow Ar^+ + Ar$	Isotropic scattering	[43]
10	$Ar^+ + Ar \rightarrow Ar + Ar^+$	Backwards scattering	[43]

and investigated by a theoretical stream–plasma interaction model. The dependence of HHs on gas pressure and driving frequency is shown in subsections 3.2 and 3.3, respectively. Concluding remarks and outlook are given in section 4. The theoretical model-related derivation, the resulting dispersion relationship, as well as the procedure for solution in the complex number domain are given in the appendix. Note that the rf frequencies chosen here are in the frequency range commonly used in space-based satellite communications [6, 32], and the pressure range investigated is also near the suggested pressure (hundreds of mTorr) in the plasma breakdown experiments [8].

2. Brief description of simulated plasma breakdown system

The plasma breakdown system investigated here is shown in figure 1, where the discharge is bounded at the left side $x = 0$ by a dielectric window. The right boundary is semi-infinite free space. This system is modeled by a kinetic PIC simulation, which is well benchmarked [34, 35] and validated by experiments [36] in low temperature plasma discharges. A large number of super-particles are used to represent a significantly higher number (10^{12} to 10^{20} m^{-3}) of time-varying physical particles. Electron–surface interactions, surface charge accumulation, volume space-charge effect, charged particle collision dynamics and transport in plasma are self-consistently considered. When a primary electron impacts the dielectric surface, secondary electrons are emitted. The corresponding SEY depends on primary electron impact energy and angle, following Vaughan's empirical formula [33], as widely adopted in the literature [2, 14, 37]. For electron impact energy E_i, and angle ξ with respect to the x direction, the SEY, δ, is given by

$$\delta = \delta_{max}(w\, e^{1-w})^k, \tag{1}$$

where $w = (E_i - E_{th})/(E_{max} - E_{th})$ with E_i the impact energy, and E_{th} the impact energy threshold, $k = 0.56$ for $w < 1$ and $k = 0.25$ for $w > 1$. If $w > 3.6$, then equation (1) is replaced by $\delta = 1.125\delta_{max}/w^{0.35}$. δ_{max} is the maximum yield and E_{max} the maximum impact energy given as below,

$$E_{max} = E_{max0}\left(1 + \frac{k_s\xi^2}{2\pi}\right) \tag{2}$$

$$\delta_{max} = \delta_{max0}\left(1 + \frac{k_s\xi^2}{2\pi}\right). \tag{3}$$

In the present work, we set $\delta_{max0} = 2.0$ and $E_{max0} = 400$ eV, and the surface is assumed to be dull, with surface smoothness factor $k_s = 1$, typically representing a material of quartz (SiO_2)

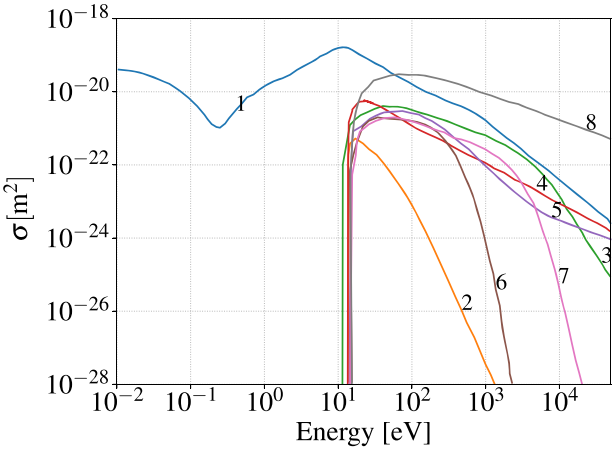

Figure 2. Cross sections for elementary processes listed in table 1. Electron–neutral and ion–neutral collisions in argon discharge.

[2]. The typical value of δ in terms of impact energy and angle is given in figure 1(b). Secondary electrons are emitted isotropically with a mean emission energy of 2 eV [6, 13].

The charged particle–neutral collisions are treated by the null-collision Monte-Carlo scheme [44]. The charged particle–neutrals interaction include e–Ar elastic scattering, impact excitation to 4s states, metastable and radiative level, 4p manifold and the highest lying states of argon, elastic scattering and resonant charge exchange for Ar^+ and Ar [45]. The corresponding reaction and its threshold are listed in table 1. The cross sections for electron–neutral collisions are given in figure 2. The cross sections for electron impact excitation to the 4s metastable and radiative argon states are taken from the collection of Hayashi [39]. In the PIC code, the cross sections for the metastable states $4s[3/2]_2$ and $4s'[1/2]_0$ are combined to give one level of Ar^m, and the cross sections for the radiative $4s'[1/2]_1$ and $4s[3/2]_1$ levels are combined into Ar^r. The cross section for electron impact excitation to the 4p manifold is taken from [40] with a threshold of 13.2 eV [Ar(4p)]. Similarly the cross sections for electron impact excitation to the higher lying manifolds are also from [40], i.e., groups II and III with threshold of 14.09 eV and 14.71 eV, respectively. The highest lying states are taken from the Hayashi collection under a threshold of 15.20 eV. In addition, long-range Coulomb interactions between charged particles are included in the simulation.

At the beginning of plasma breakdown, the plasma densities are relatively low. We employ a spatially uniform electric field, which is parallel to the surface, following the external rf field configuration utilized by Lau *et al* [27] and Zhang *et al* [26]. Here the electric field in the y direction is $E_y = E_{rf0} \sin 2\pi ft$ with E_{rf0} the transverse electric field amplitude. It is worth noting that the initial phase of rf electric field can play an important role for the special normal resonant multipactor [46] for oblique rf electric field. Here, the rf electric field is tangential to the surface, and the initial phase will bring an overall phase shift for the discharge, and has little effect on the main physics of HH investigated here. Therefore, the initial phase is fixed at zero. The charged particles are pushed by both transverse and normal electric field, E_y and E_x. The magnetic motion of charged particles is neglected due to the much weaker magnetic component and its larger Lagmour radius than the discharge size. The time step is $\Delta t = 10^{-14}$ s for $f = 1$ GHz. For higher frequency cases, Δt is changed to keep $f\Delta t$ constant, accordingly, which guarantees sufficient time resolution for all cases. The charged particles flowing to the dielectric surface are instantaneously accumulated.

3. Results

3.1. Higher harmonic generation at base case

In this subsection, we present the main physics of HHs [29] in detail through a base case with the driving frequency $f = 1$ GHz, amplitude of rf transverse electric field, $E_{rf0} = 3$ MV m^{-1}, and background gas 0.2 Torr. These discharge conditions at base case are the same as that in [29]. Note that the multipactor ionization breakdown experiments suggested a gas pressure around hundreds of mTorr [8], and the pressure range chosen here and investigated in the next section is near the value suggested in the experiments. Part of the materials for figures 3–6 are based on our short letter [29]. For the sake of completeness to show more detailed physics of the HH phenomenon and provide background for the later discussion, we show them as the base case of this work.

Figures 3(a) and (b) show the spatiotemporal normal electric field, E_x, and ion density, n_i, respectively. At the beginning of the discharge, the multipactor avalanche emission dominates, E_x rapidly increases first and then oscillates periodically at twice the fundamental rf frequency (1 GHz), which is similar to the previously reported vacuum multipactor process [12, 14]. The normal electric field is positive, i.e., it points away from the dielectric window surface and gradually decreases in space because of the shielding effect of space charge. Meanwhile, the electron–neutral impact ionization creates more and more e–ion pairs, resulting in the formation of plasma as figure 3(b) shows. Fast oscillations in time, i.e., the enhanced HHs of E_x (also other plasma quantities, see figures 4 and 5 later) are observed. To explicitly visualize the oscillations, figure 3(c) shows the locally zoomed electric field outlined by the red rectangle in figure 3(a), and temporal E_x/E_{rf0} near $x = 12$ μm is displayed in figure 3(d), where the red line shows the normalized rf electric field E_{rf}/E_{rf0} over time. Quantitatively, the HH frequency is around 10 GHz, ten times the rf frequency, but lower than the Langmuir frequency of plasma–electron oscillation (around 10^2 GHz). Such kind of oscillations roughly start from $t/T \approx 6$ and its oscillating amplitude increases over time (see black line in figure 3(d)). As figure 3(a) shows, such fast oscillating E_x mainly locates in region (II), which is a transition region from the region (I) (multipactor dominant) to region (III) (bulk plasma region), and weakly appears in region (III) and (IV). It is around 20 μm long for the region where the longitudinal oscillating electric field appears. The value of $E_x = 0$ V m^{-1} is indicated by the dashed line in black in figure 3(a), implying the transition boundary of the electric field direction, which is used to define

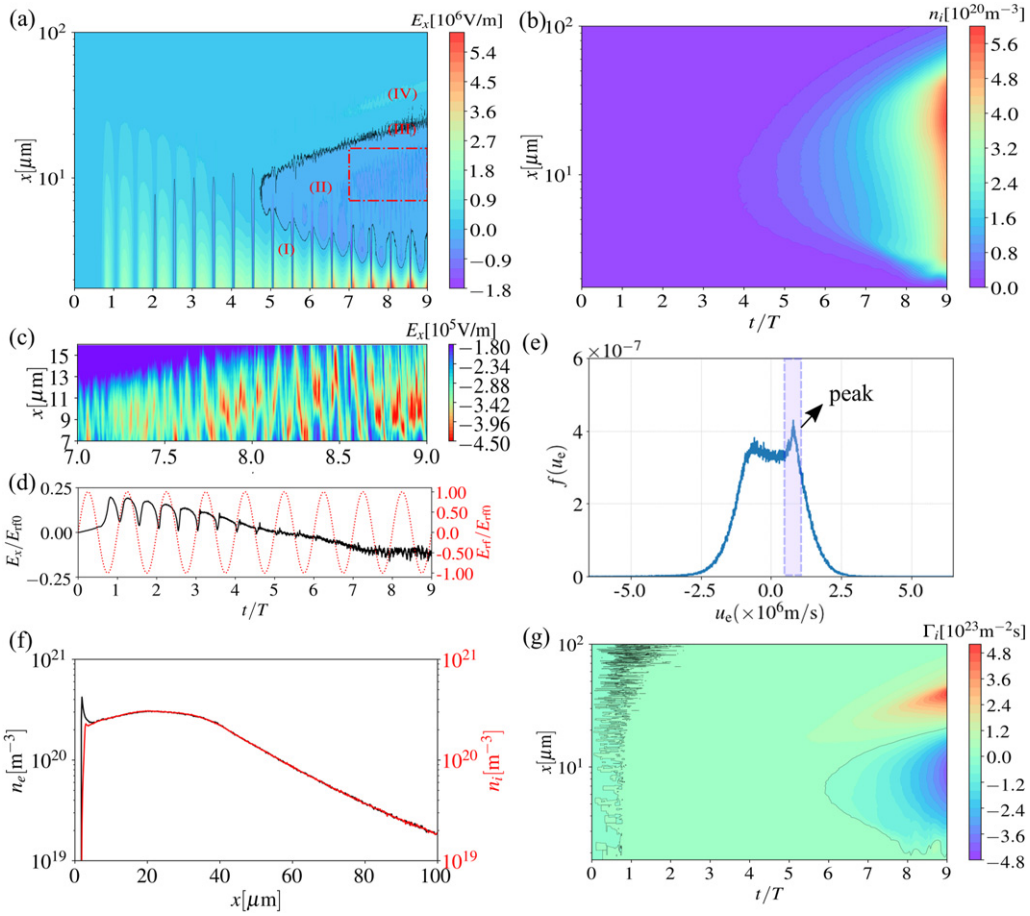

Figure 3. Spatiotemporal (a) normal electric field, E_x, (b) ion density n_i, (c) locally zoomed normal electric field, E_x, (d) the normalized transverse rf field (red dashed line), E_y/E_{rf0}, and E_x/E_{rf0} at $x = 12$ μm, (e) the smoothed electron velocity distribution function normalized to the total electron density, (f) the space-dependent electron and ion density distribution at $t/T = 8$, (g) the spatiotemporal ion flux Γ_i. (a), (c), (d) and (f) Reprinted figure with permission from [29], Copyright (2022) by the American Physical Society.

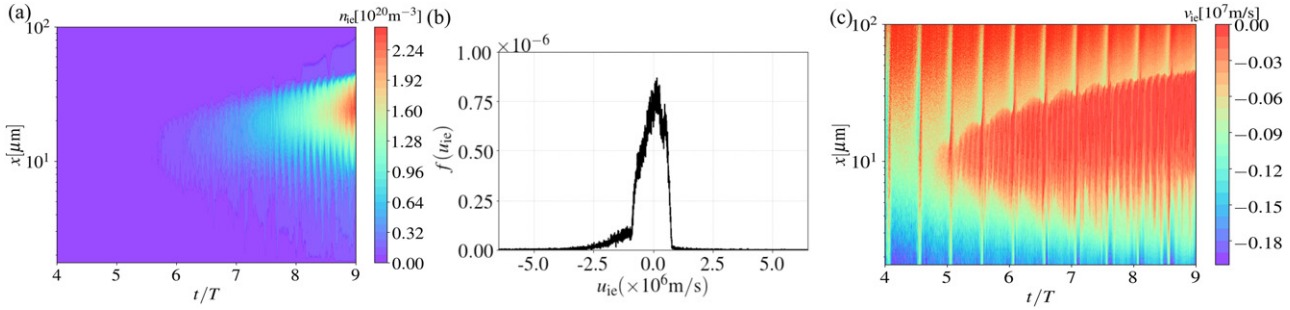

Figure 4. (a) The spatiotemporal ionization electron density; (b) the corresponding smoothed velocity distribution function of the ionization electron near $x = 12$ μm and $t/T \approx 7$; (c) the spatiotemporal ionization electron fluid velocity. (a) and (b) Reprinted figure with permission from [29], Copyright (2022) by the American Physical Society.

the boundary for the multipactor region (I) ($E_x > 0$), the transition region (II) ($E_x < 0$) and plasma bulk region (III) $E_x \approx 0$, and region (IV) $E_x > 0$. With the discharge evolving in time, the multipactor region is gradually reduced, as the increasing ion density shows in figure 3(b). A very short time duration, for which the normal electric field is negative in region (I) (see figure 3(a)), is also found when $2t/T$ is around an integer. In this time duration, as shown by the red line in figure 3(d), the transverse electric field is around zero, and hence the primary electrons returning to the surface have a small impact energy, giving rise to less intense secondary electron emission, i.e., SEY is less than unity (see figure 1(b)) and negative charge is accumulated on the surface. At other times, the transverse electric field is strong and the impact energy is higher, thus, the secondary electron emission is sufficiently intense to give multipactor growth.

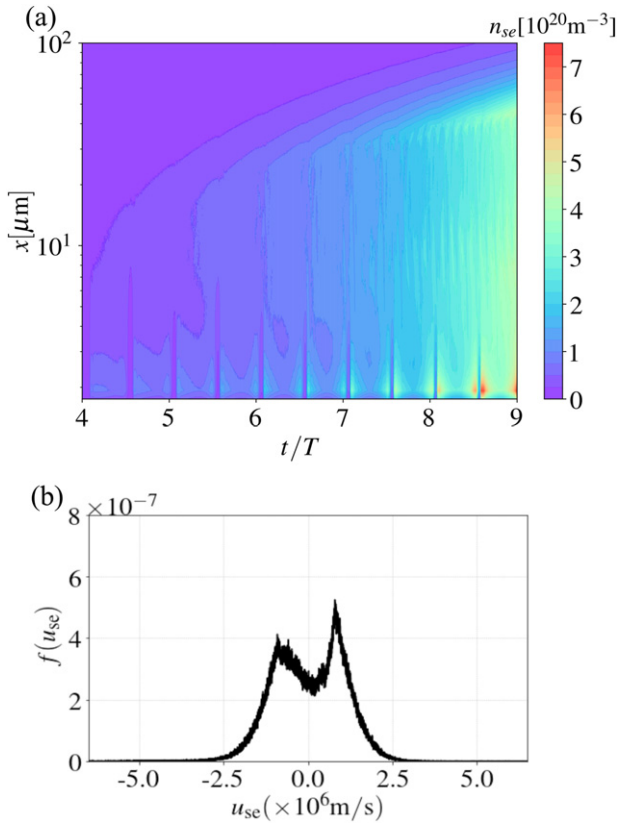

Figure 5. (a) The spatiotemporal secondary electron density, (b) the corresponding smoothed velocity distribution function of the secondary electron near $x = 12$ μm and $t/T \approx 7$. Reprinted figure with permission from [29], Copyright (2022) by the American Physical Society.

The smoothed electron velocity distribution function at $x = 12$ μm and $t/T \approx 7$ is presented in figure 3(e). As shown by the arrow, there is a local peak near $u_e \approx 10^6$ m s^{-1}. The origin of this peak and its important role will be discussed in more detail later.

Figure 3(f) shows the electron and ion density distribution in space at $t/T = 8$. We can see that near the surface the ion density is significantly lower than the electron density. In general discharges bounded by dielectric or metal surface, an ion sheath with electron density lower than ion density forms, and the electric field inside points toward the surface to repeal electrons and attract ions. However, here an electron sheath is formed, and the local high multipactor electron charge within the sheath leads to a positive E_x in region (I) and an opposite E_x in region (II). It is attributed to two aspects: firstly, the dense secondary electron emission due to energetic primary electrons impact on the surface, temporarily localizes near the surface; secondly, abundant electron–neutral impact ionization events in the plasma region (III) produce more and more electrons that diffuse toward the surface under the action of electron density gradient. We can also see a small region near the dielectric surface, where the ion density significantly decreases. This is because the ions are slowly repelled away from the surface by the positive restoring field in region (I), especially near the surface. The collective motion of ions can be revealed by the ion flux, $\Gamma_i = n_i v_i$, with n_i shown in figure 3(b) and v_i the ion fluid velocity, in figure 3(g). Again, the black dashed line represents the spatiotemporal field reversal boundaries. Clearly, the ions move collectively on a slow time scale and are not responding to the fast oscillating HH electric field. Ions always flow away from the surface in the initial several rf periods, and then flow toward the surface and to free space from both sides of the plasma region (III), respectively. The presence of the reversed ion flux distinguishes the ionization plasma discharges from the vacuum electron multipactors.

The nature of this HH generation is analyzed based on simulation data and a theoretical model. As mentioned above, ions are almost immobile compared to electrons during an rf period due to their large mass. Therefore, the appearance of HHs in this short time scale is linked to the dynamic of electrons. The electrons are labeled by production source: the surface-emitted electron is tagged as secondary electron (se), and that from impact ionization event is tagged as ionization electron (ie). The spatiotemporal ie density is shown in figure 4(a). Here the time range of t/T shown is from 4 to 9 in order to emphasize the special new physics, the well-known multipactor part within $0 < t/T < 4$ similar to the vacuum multipactor discharges is not shown. Its corresponding velocity distribution function, f (u_{ie}), measured in PIC simulation is revealed in figure 4(b), where u_{ie} is the velocity of individual ionization electrons. Integrating the product of velocity u_{ie} and velocity distribution function $f(u_{ie})$ over all the particles, gives the electron fluid velocity, $v_{ie} = \int_{-\infty}^{+\infty} u_{ie} f(u_{ie}) \mathrm{d}u_{ie}$, which is plotted in figure 4(c) as a function of time and space. Clearly, both the density and fluid velocity of ie exhibit fast oscillations in time. As shown in figure 4(b), it is worth noting that the profile of $f(u_{ie})$ is similar near $x = 12$ μm and for the time duration of $7 < t/T < 9$. Here only the typical results of 'ie' for $x \approx 12$ μm and $t/T \approx 7$ are shown. Near this location and time instant, the ionization electrons move at a small net negative drift velocity $v_{ie0} \approx -1 \times 10^5$ m s^{-1}, implying that the 'ie' drifts slightly towards the surface. Similarly, the spatiotemporal plot of secondary electron density is shown in figure 5(a), and the velocity distribution function, $f(u_{se})$, in figure 5(b). Again, remarkable HH oscillations for 'se' appear. $f(u_{se})$ shows two narrow peaks, i.e., a fraction of the se ($u_{se} > 0$) are injected into the plasma, and the other group of electrons ($u_{se} < 0$) are leaving plasma towards the surface. Clearly, we can see that the narrow peak ever observed in figure 3(e) is originally from these secondary electrons. The secondary electron velocity distribution function $f(u_{se})$ is very similar to an ideal Dirac δ-function for $u_{se} > 0$. Thus, a cold electron stream for secondary electrons injecting into plasma could be modelled and it interacts with ionization electrons.

Next, we model the cold stream–plasma interaction system by treating the secondary and ionization electrons as fluids in collisional regime. As discussed above, the argon ions are almost immobile, and the dense electrons above the surface shield the restoring field from surface charge, implying that it hardly affects the stream–plasma interaction. If the cold secondary electrons have a fluid drift velocity v_{se0} and density n_{se0}, and propagate into a plasma consisting of ionization electrons, which have a fluid velocity v_{ie0} and density

n_{ie0}, electron–neutral momentum transfer frequency, ν_m, and thermal temperature T_{iexx} in the x direction, then, we derive the dispersion equation of the stream instability-induced fast HH oscillation for a system of a cold stream–plasma interaction. Let us describe the total temporal oscillating quantities generally:

$$A = A_0 + \tilde{A}\, e^{\,j(kx-\omega t)}, \tag{4}$$

where A_0 represents slowly varying quantities in time like ionization electron density (n_{ie0}), fluid velocity (v_{ie0}), etc, and $\tilde{A}\, e^{\,j(kx-\omega t)}$ denotes the fast oscillating part, then the phenomenon of HH oscillation can be characterized by the frequency Re(ω), growth rate Im(ω) of the HH oscillation amplitude, and wavenumber k. Here, Re(ω) and Im(ω) represent ω's real and imaginary part, respectively, and j is the unit imaginary number. We obtain the dispersion expression for HH oscillations [29] as follows (see appendix for more detail)

$$1 = \frac{\omega_{ie0}^2}{(\omega - kv_{ie0} + j\nu_m)(\omega - kv_{ie0}) + k^2 k_B T_{iexx}/m} + \frac{\omega_{se0}^2}{(\omega - kv_{se0})(\omega - kv_{se0})} \tag{5}$$

with $\omega_{ie0,se0}^2 = e^2 n_{ie0,se0}/m\epsilon_0$. The procedure to solve it in complex number domain is also presented in the appendix. If we assume that the ionization electrons are cold ($T_{iexx} = 0$) and there are no electron–neutral collisions ($\nu_m = 0$), the above equation reduces to the classical dispersion relationship of two stream instabilities (see more detail in reference [47]).

As the HH frequency is much higher than the fundamental rf frequency, the varying physical quantities in terms of the fundamental frequency rf electric field are treated as slowly varying quantities, and we can obtain their values by filtering the HH oscillation. As a result, the slowly varying ionization electron density n_{ie0}, fluid velocity v_{ie0}, and thermal temperature in the x direction, T_{iexx}, and secondary electron density n_{se0} are shown in figure 6(a). v_{se0} is kept around 10^6 m s^{-1}. Typically, for $t/T \approx 7$, we have the following parameters: $n_{ie0} = 2.96 \times 10^{19}$ m^{-3}, velocity $v_{ie0} = -1.16 \times 10^5$ m s^{-1}, and $n_{se0} = 5.04 \times 10^{19}$ m^{-3}. The effective ionization electron momentum transfer frequency is measured in the simulation by recording all the collisions, and it has a value of $\nu_m = 0.7 \times 10^9$ s^{-1} and $T_{iexx} = 2.67$ eV. Substituting the above parameters into equation (5), we get the oscillating angular frequency Re(ω), growth rate Im(ω) as a function of varying wavenumber k, as exhibited by the solid line in figure 6(b) for $T_{iexx} = T_{iexx}|_{PIC}$ (2.67 eV near $t/T = 7$ for PIC simulations). Here, the left axis is the real part of ω, Re(ω) (black line), and right vertical axis denotes the imaginary part Im(ω) (red line), respectively, and the solid blue line indicates the maximum Im(ω), labeled as P_1, the corresponding wavenumber, k_{max}, gives the dominant mode of longitudinal oscillations. The value of Im(ω) at P_1 has a growth rate around 0.3 GHz at given plasma frequency (see solid red line in figure 6(b)). The real part Re(ω) at k_{max}, shown by point P_2, determines an oscillation frequency around 10 GHz, the same as that of kinetic simulation. Meanwhile, a wavelength of $2\pi/k_{max} \approx 10$ μm, close to the value from the simulation for the longitudinal oscillation, is obtained. In figure 6(b), we also show the effect of ionization electron temperature on the growth rate and the

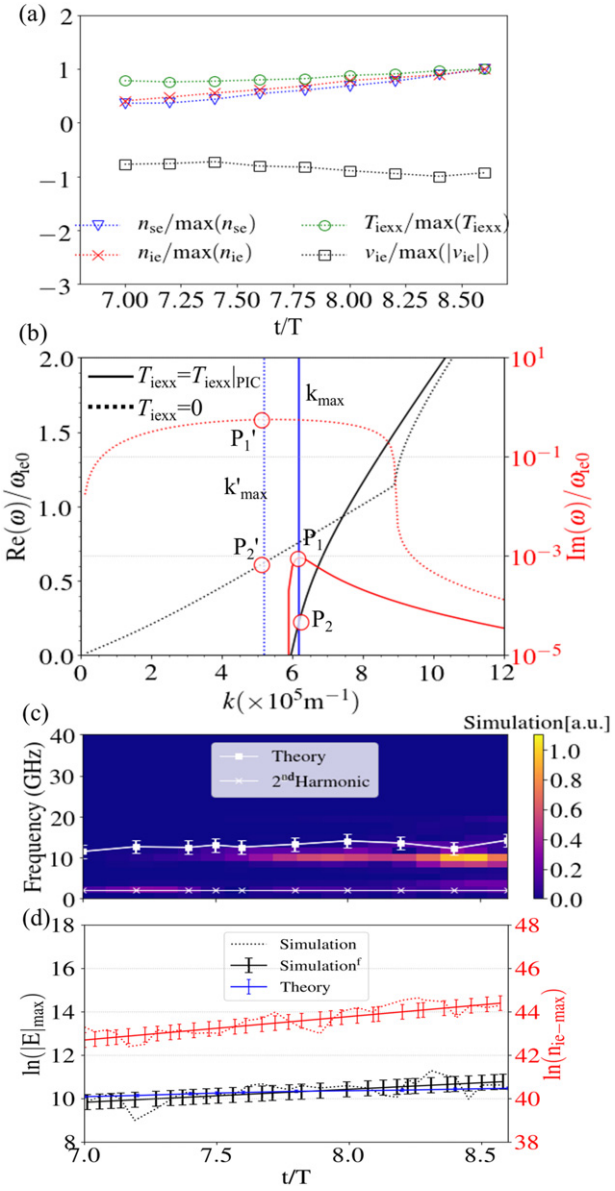

Figure 6. (a) The slowly varying secondary electron density n_{se}, ionization electron temperature T_{iexx} in x direction, ionization electron density n_{ie} and fluid velocity v_{ie}, here $\max(n_{se}) = 1.38 \times 10^{20}$ m^{-3}, $\max(T_{iexx}) = 3.4$ eV, $\max(n_{ie}) = 7.25 \times 10^{19}$ m^{-3}, $\max(|v_{ie}|) = 1.5 \times 10^5$ m s^{-1}. (b) Dispersion relationship solution for $T_{iexx} = T_{iexx}|_{PIC}$ (solid line) and 0 (dashed line), real and imaginary part of ω, Re(ω) (black line) and Im(ω) (red line), as a function of real wavenumber k, and the maximum Im(ω) at point P_1 (and P_1') is indicated by the vertical solid (dashed) blue line, and the corresponding Re(ω) is displayed at point P_2 (and P_2'). (c) The temporal frequency spectrum of E_x within the time duration of 7.0–8.6 rf periods. The relative strength of oscillation at different frequencies is indicated by the brightness. The rectangle line in white shows the oscillation frequency from theory, (d) the time-varying amplitude of oscillating electric field and ionization electron density from theory (solid blue line) and simulation (dashed black line), and a linear fit of the simulation results (solid black line). (b)–(d) Reprinted figure with permission from [29], Copyright (2022) by the American Physical Society.

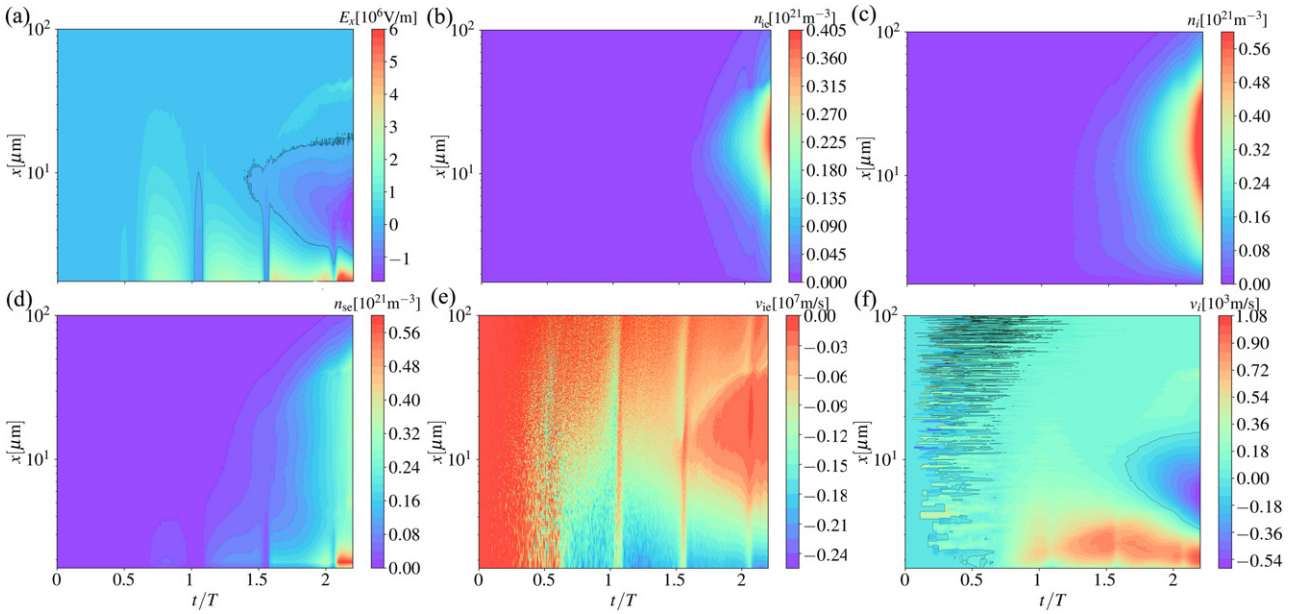

Figure 7. Spatiotemporal (a) normal electric field, (b) ionization electron density, (c) ion density, (d) secondary electron density, (e) ion fluid velocity, (f) charge density at 1 Torr, 1 GHz, and 3 MV m^{-1}.

fast oscillation frequency by setting $T_{\mathrm{iexx}} = 0$ as shown by the dashed red and black lines. Similarly, the corresponding values are labeled by the point P_1' and P_2'. One can see that the growth rate for $T_{\mathrm{iexx}} = 0$ is much larger than that at $T_{\mathrm{iexx}} = T_{\mathrm{iexx}}|_{\mathrm{PIC}}$ by two order of magnitude, and the oscillating frequency is also higher by a factor of around 3, indicating the importance of ionization electron temperature considered in our theoretical model. In addition, a small broadening exists for the secondary electron velocity distribution function (figure 5(b)), $f(u_{\mathrm{se}})$, compared to an ideal delta function, therefore, we also examined the response of the wavenumber, growth rate and oscillation frequency to the deviation of the electron fluid velocity and density. It turns out the results are robust for properly varying input parameters within $\pm 10\%$. Its thermal effect is also examined by adding an additional term representing secondary electron thermal temperature in equation (5). Let us assume that the secondary electrons have a temperature of 0.5 eV for the broadening of $f(u_{\mathrm{se}})$ in figure 5(b), roughly equivalent to the half of the broadening of $f(u_{\mathrm{ie}})$ in figure 4(b), then the oscillation frequency is found to be around 14 GHz, and the growth rate is 0.15 GHz, still in reasonable agreement with the PIC simulation. Therefore, even though the theoretical model presented here is simplified, the good agreement between the model and the simulations convinces us its capability capturing the mechanism of the PIC observations.

The temporal frequency spectrum of E_x from PIC simulation near $x = 12$ μm is shown in the contour plot of figure 6(c). The contour is obtained by a moving window in time, which is 64% of a rf period. Two successive windows have a 78% overlap. The most significant components of the HH are around 10 GHz. The brightness of the contour represents the magnitude of the oscillating electric field at the resulting frequencies. The second harmonic frequency [14, 31] is also captured as the electrons collectively respond to the rf electric field. The electrons 'see' the magnitude of the rf transverse electric field, rather than the phase for successive electron–neutral (and/or electron–surface) collisions. The theoretically calculated oscillation frequency, $\mathrm{Re}(\omega)/2\pi$, via substituting the slowly varying (unperturbed zero order) quantities of figure 6(a) into equation (5), gives the rectangle line with error bar of the mean standard deviation in figure 6(c). The error bar is obtained by using the ie fluid velocity v_{ie0} within 10% difference. We can see that the maximum deviation between theory and simulation is within 30%, revealing a good agreement. On the other hand, the resulting amplification of HH amplitude oscillates as a function of time, whose slope represents the growth rate $\mathrm{Im}(\omega)$, is shown in figure 6(d). Here, $|E|_{\mathrm{max}}$ is the amplitude of the HH oscillation filtering the slowly varying electric field. The black dashed line represents the results from PIC simulation, and its linear fitting, which gets rid of the noise induced by the limited number of particles, is presented by the solid line in black. The mean standard deviation showing the difference of the fitted curve from the PIC data is indicated by the error bar. The blue dashed line shows the amplitude in theory, again with an error bar representing the standard deviation for $v_{\mathrm{ie0}} \pm 10\%$. Clearly, a very good agreement is obtained between the PIC simulation and the theory. Similar to $|E|_{\mathrm{max}}$, the amplitude of HH oscillating ionization electron density, n_{iemax}, is shown by the red lines. We can see that the growth rate of the density amplitude is similar to that of normal electric field. The relative deviation between them is around 30%, which is because the oscillating amplitude in simulations is a superposition of a few high frequency components in addition to the single frequency 10 GHz (see figure 6(c)).

Here the effective momentum transfer frequency used in the theoretical model is based on the statistics from the PIC simulation via collecting the collision numbers in the Monte

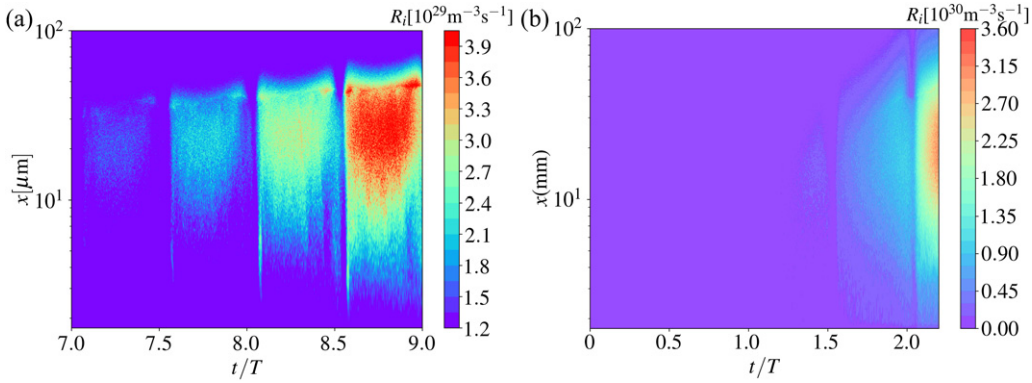

Figure 8. The spatiotemporal ionization rate for (a) base case at 0.2 Torr and (b) 1 Torr.

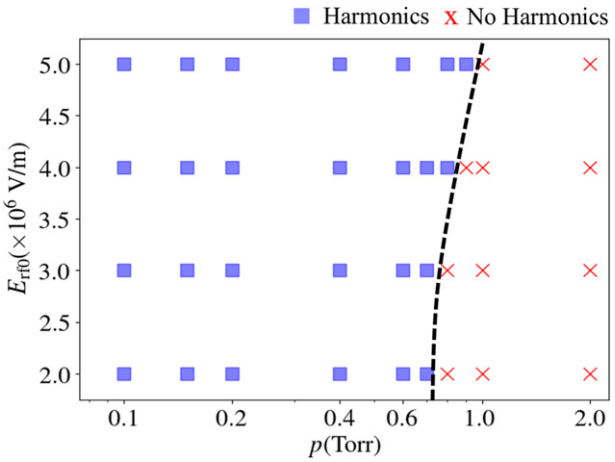

Figure 9. Phase diagram of the presence/absence of high harmonics measured from the PIC simulations at 1 GHz. The blue boxes indicate the region in which HHs are observed, and red crosses represent the absence of HHs. The dashed black line is the boundary.

Carlo module. The calculation of ν_m for fluid model based on PIC simulation has attracted interest in recent years [48–50], and it has been found that different methods, i.e., $n_g\langle\sigma_m u\rangle$ against $n_g\langle\sigma_m u u_x\rangle/\langle u_x\rangle$ where σ_m is the elastic momentum transfer cross section, u is the speed of individual particle and u_x is the x component of the velocity, $\langle\cdot\rangle$ means averaging over the distribution function, can lead to a difference of factor up to 2 in rf discharges for a Ramsauer gas like argon, the difference mainly comes from the stochastic thermal motion of all the electrons, which will affect the fluid results for momentum loss and overall electron power absorption. In our theoretical model, we have examined the effect of different collision frequency, and it turns out the results in our scenario weakly depend on the collision frequency in the parameter range of interest. When we increase ν_m to $2\nu_m$, the change of the oscillation frequency is only around 25%, and the growth rate increase by a factor of 2 (closer to the simulation). The physical reason of why the oscillation frequency and growth rate weakly depend on the collision frequency in the parameter range investigated here, is that the secondary electron has a property of a cold beam.

One more interesting phenomenon observed is the roughly unchanged HH frequency in time. The slowly increased ionization electron density results in a higher electron plasma frequency, ω_{ie}, which is expected to induce a higher HH frequency if other conditions kept unchanged. However, as we see in figure 6(a), the ionization electron temperature, T_{iexx}, is also slowly increasing in time, thus, it takes more time for them to collectively move back and forth during the fast oscillation grows up, resulting in a lower HH frequency. This physics is also theoretically proved by equation (5), as the shown in figure 6(c).

In addition, we also observe the spectrum at roughly twice of the enhanced HH frequency, around 20–25 GHz in the simulation, which is not shown here due to the much smaller amplitude. This may be attributed to the higher order terms currently excluded in the theoretical model.

3.2. Pressure effect

In order to explore the pressure effect, in this subsection, firstly, we extend the base case to a case of higher pressure at 1 Torr with the amplitude of the transverse rf electric field and the driving frequency kept at 3 MV m^{-1} and 1 GHz, respectively.

In figures 7(a)–(f), the spatiotemporal normal electric field, E_x, ionization electron density, n_{ie}, ion density, n_i, secondary electron density, n_{se}, ionization electron fluid velocity, v_{ie}, and ion fluid velocity, v_i are shown, respectively. Compared to the base case, the ionization breakdown is much faster and the ion density increases to 6×10^{20} m^{-3} within 2.2 ns, which is consistent with the scaling law of discharge formation time versus pressure in [27]. Lau *et al* [27] found the discharge formation time as a function of pressure decreases first and then increases with the inflection occurring between 10–50 Torr. Here, the cases investigated are in the left branch of the curve.

In addition to the overall physics, more detailed spatiotemporal features are also revealed at higher pressure. Clearly, the normal electric field in figure 7(a) shows a similar behavior as the base case in the first rf period, i.e., E_x is always positive due to the secondary electron emission as in figure 7(d). Within the second rf period, plasma density (see n_{ie} and n_i in figures 7(b) and (c)) starts increasing rapidly in time, and a bulk plasma

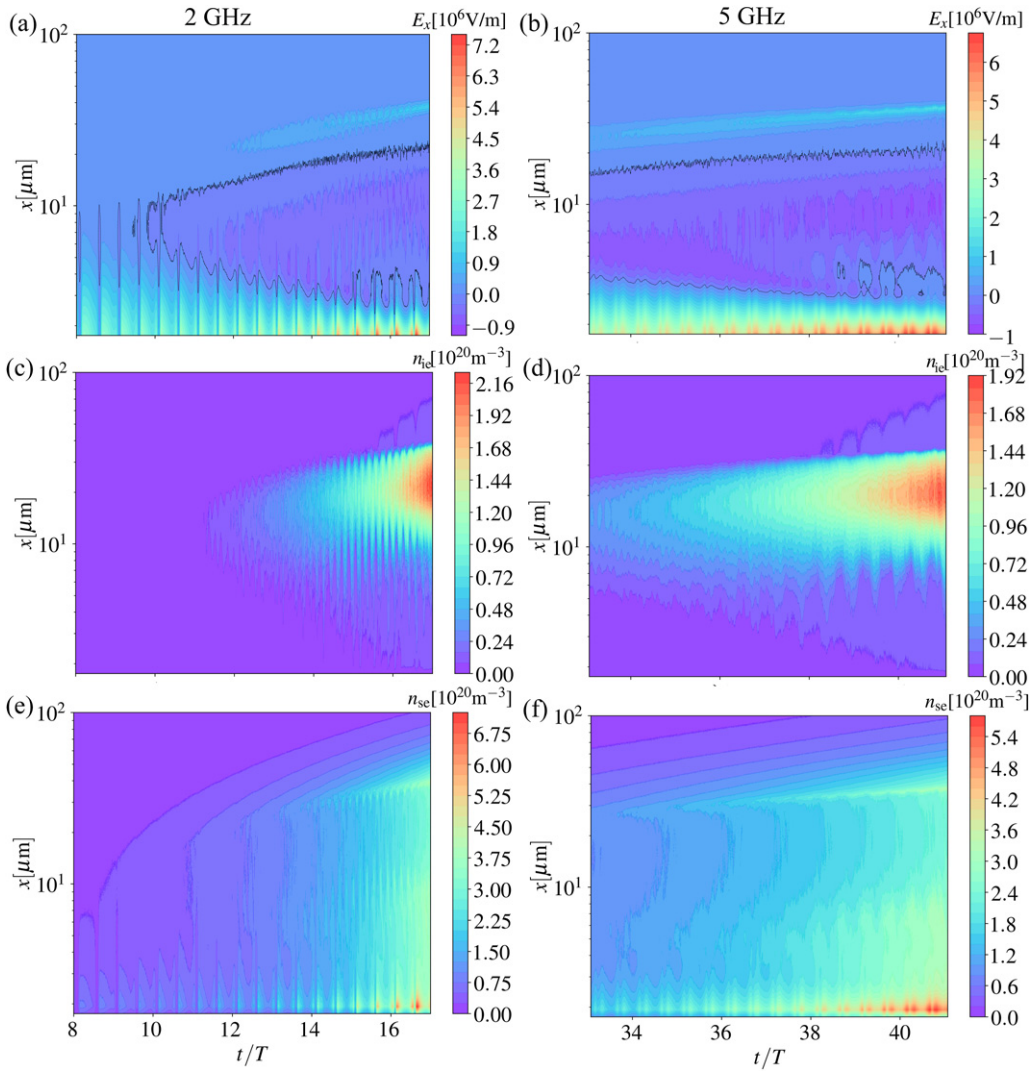

Figure 10. Spatiotemporal (a) electric field (c) ionization electron density (e) secondary electron density at 2 GHz; (b) electric field (d) ionization electron density (f) secondary electron density at 5 GHz.

region appears near $x = 20$ μm. Two diffusion regions bounding the bulk plasma region are also observed. Additionally, the secondary electron density continues increasing in the multipactor region, which induces a significantly enhanced restoring field near the surface. Under the action of this restoring field, the ionization electrons are accelerated toward the surface and induce more secondary emission. A positive feedback, the secondary electron density keeps increasing in the early stage of the discharge formation. Meanwhile, as shown in figure 7(f), the ions are repelled from the dielectric surface. More importantly, the HH oscillations for E_x, n_{ie}, n_{se} and v_{ie} vanish at 1 Torr. One reason for the reduced HH oscillations is the secondary electron velocity distribution function $f(u_{se})$ deviating from a beam-like δ-function with a broadening due to more frequent collisions. The other important reason is that the ionization electron density rapidly increases within a small time scale, and there is insufficient time for fast oscillations to grow. The spatiotemporal ionization rate, R_i, for 0.2 Torr and 1 Torr is shown in figures 8(a) and (b), respectively. The maximum value of R_i at 1 Torr is around eight times higher than that at 0.2 Torr. A less significant fast oscillation is observed for 0.2 Torr. This is because the modulation of the normal electric field will accelerate and deaccelerate electrons, leading to a modulation of electron energy, which in turn, gives rise to rapidly oscillating electron–neutral collision rate. The excitation rates have behaviors similar to the ionization rate (not shown here). The ionization rate R_i almost monotonously increases within one rf period.

To reveal the dependence of HH oscillations on the background pressure, additional simulations scanning the amplitude of the rf electric field in range of 2–5 MV m^{-1}, and pressure in range of 0.1–2 Torr, are performed. The resulting diagram of the presence of HH oscillation is revealed in figure 9. A transition boundary from the presence to the absence of HH is found near 0.8 Torr by quantitatively examining if the normalized HH amplitude higher than 10%. Note that the HH amplitude is normalized to the amplitude of the fundamental frequency oscillation.

The transition boundary revealed by the black dashed line sits near 0.8 Torr and changes slightly for various amplitudes

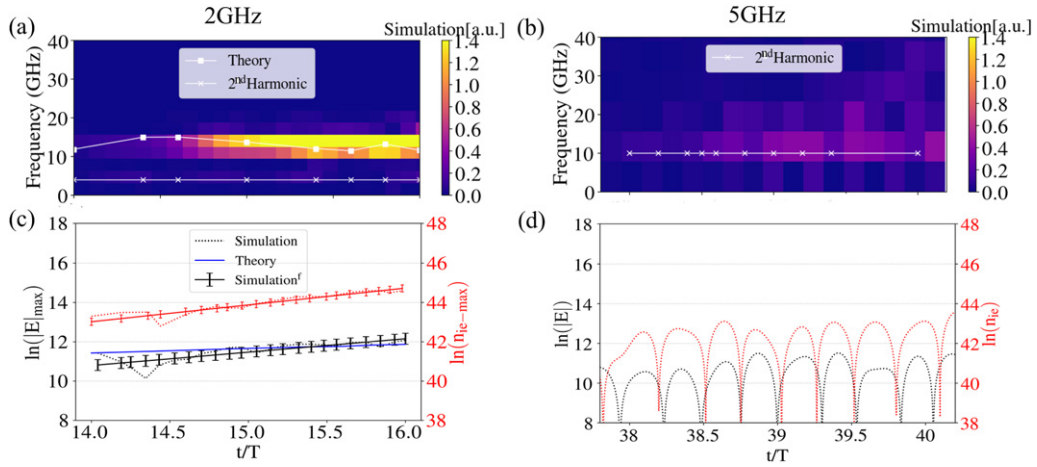

Figure 11. The temporal frequency spectrum of E_x over time range of $14 < t/T < 16$ for (a) 2 GHz and $38 < t/T < 40$ for (b) 5 GHz. The color brightness represents the relative strength of the magnitude of oscillating E_x at different frequency spectrum. The time window, and its overlap between successive windows are same as figure 6(c). The white rectangle and star lines show the HH frequency from theory and its second harmonic, respectively, for the case of 2 GHz and the only second harmonic at 5 GHz. (c) The theoretical time-varying amplitude of HHs (solid blue line) and simulation results (dashed line) as well as its linear fitting. (d) The time varying electric field and ionization electron density in time after subtracting slow variations from E_x and n_{ie}.

of transverse electric field. As mentioned above, higher ionization collision rate restricts the development of the instability. The ionization collision rate can be estimated by $N\sigma(\epsilon_{ie})v_{ie}$ [44] with N the density number of neutral atoms and v_{ie} the total speed of individual electron, and ϵ_{ie} the electron kinetic energy. $\sigma(\epsilon_{ie})$ is the collision cross section, which is shown in figure 2 for each kind of electron–neutral collision. We can see that the cross section decreases with electron kinetic energy (equivalent to the speed of an individual electron) when the electron energy exceeds a certain value. In the process of high electric field breakdown, the electron kinetic energy is mainly determined by the amplitude of transverse electric field (E_{rf0}), and it is can be relatively high. Thus, higher electric field tends to give rise to higher electron speed, but lower ionization cross section. Ultimately, $N\sigma(\epsilon_{ie})v_{ie}$ is less sensitive to E_{rf0}. Therefore, the transition boundary changes slightly for various E_{rf0}.

It is worth noting that the time range discussed for 1 Torr is different from that for the base case of 0.2 Torr. Again, we focus on the particular physics of enhanced harmonics, which is highly relevant to plasma density rather than the absolute time. For the frequency effect, that will be discussed in the next section, we also investigate the HH phenomenon for plasma density near 10^{20} m^{-3}.

3.3. Driving frequency effect

In this section, we explore the effect of the driving frequency on HH oscillations. The spatiotemporal normal electric field E_x, ionization electron density n_{ie}, and secondary electron density n_{se} are shown in the first column for 2 GHz and second column for 5 GHz in figure 10, respectively. The corresponding time duration chosen for 2 GHz is over the range of $8 < t/T < 17$. For the case of 5 GHz, we show the results within $33 < t/T < 41$. For both cases, the maximum ionization electron density increases to a value near 2×10^{20} m^{-3}, which is very close to the base case. We choose the discharge stage, within which n_{ie} is almost the same, thus, the effect of driving frequency is highlighted. It can be found that, even though the discharge experience different number of rf periods to have a similar plasma density, the absolute discharge time is almost the same, i.e., 8–9 ns. In figures 10(a), (c) and (e), obviously, HH oscillations are observed in both PIC simulation and theory for $f = 2$ GHz. However, at 5 GHz, the normal electric field and ionization electron density oscillate only at twice fundamental frequency, which has been revealed as the second harmonic in figure 6(c). That implies the longitudinal quantities collectively move, following the fundamental frequency oscillation. By plotting the temporal spectrum of E_x for 2 GHz, again, we get the HH frequency near 10 GHz with a slightly broadening distribution of the frequency spectrum in figure 11(a). In figure 11(b), the temporal frequency spectrum is given for $f = 5$ GHz. As the brightness represents for the strength of the HH oscillations, thus, the HH oscillations with a frequency of 10 GHz indeed is significantly reduced at $f = 5$ GHz. The corresponding amplitudes of the HH oscillating E_x and n_{ie} for 2 GHz are shown in figure 11(c). Note that the slowly varying E_x and n_{ie} are taken off by filtering the low frequency component below 6 GHz. A reasonable agreement between PIC simulation and theory is obtained for the amplified amplitude of the HH oscillations. For $f = 5$ GHz, adapting a similar treatment as figure 11(c), we plot the absolute value of normal electric field and ionization electron density, labeled as $|E|$ and n_{ie}, as a function of time. As we can see that $|E|$ and n_{ie} follow the slow fundamental oscillation in a time scale of rf period. This is because the slowly varying quantities like n_{ie0}, v_{ie0}, n_{se0} etc mainly modulated by the fundamental oscillations. It is worth noting that in figure 11(d), the $\ln|E|$ and $\ln(n_{ie})$ oscillate at four times fundamental frequency, this is because of the way we plot the data, which subtracts the slow fundamental oscillations, thus the peaks and valleys of the fundamental oscillations bring an additional second harmonic oscillations.

In addition, we explore the case $f = 0.5$ GHz, which is found to be similar as the cases $f = 1$ and 2 GHz. For higher driving frequency $f = 10$ GHz, there is no enhanced frequency spectrum found over the range of 0–40 GHz, and only certain oscillations near electron plasma frequency are observed (not shown here).

4. Concluding remarks and discussions

In summary, the HH content of the longitudinal physical quantities normal to the surface, including the normal electric field, electron density, electron impact ionization and excitation rate, in the early stage of HPM plasma breakdown near a dielectric surface is studied in detail. By developing a theoretical model, the mechanism of the excited HH generation is found to be attributed to the two opposing electron streams-induced instability, i.e., the interaction between beam-like secondary electrons, and ionization electrons in the plasma. The HH oscillation frequency, amplification of the HH oscillation amplitude, as well as wavenumber in theory agree well with the simulations. The HH oscillation is significantly reduced at higher pressures due to higher ionization rate, which leaves little time for instability to grow. Furthermore, the diagram of the presence of HH oscillation is revealed for various transverse electric field amplitudes, E_{rf0}, and background gas pressures, p. The transition boundary regarding pressure for various E_{rf0} is around 0.8 Torr. The transition pressure changes slightly for various amplitudes of transverse electric field. Finally, the effects of the driving frequency on HH oscillations are investigated in range of 1–5 GHz. For cases of 1 and 2 GHz, and HH oscillation frequency and the growth rate of HH oscillating amplitude are close to each other, with values of around 10 GHz and 0.3 GHz, respectively. With further increasing the driving frequency to 5 GHz, the HH oscillations are found to be significantly reduced again, because only slowly varying normal electric field and electron density are present, which are determined by the modulation of the fundamental frequency.

The HH oscillations are expected to vary for surface materials with different surface SEY properties, as well as electronegative gases like SF_6, which may also be utilized in space-based microwave transmission systems due to their suppressive properties. This would affect the electron density and secondary electron emission and therefore the HHs generation during plasma breakdown. The enhanced HH components and its underlying regime revealed in this work imply that a new form of rf signal may be generated and some form of new diagnostic based on electric field spectrum may be potentially developed for the transient breakdown physics within one rf period. The enhanced HH spectrum is absent in the multipactor-dominant stage, for example $0 < t/T < 6$ at the base case, and it appears only in the transition from multipactor to rf plasma, where the plasma density is around 10^{20} to 10^{21} m^{-3}, thus, the detection of the enhanced HH spectrum has a potential to be a indicator for ionization breakdown in multipactor-coexisting plasma breakdown process at similar external conditions, i.e., the gas pressure is tens to hundreds of mTorr and rf frequency around 0.5–2 GHz. In addition, the fast-oscillating HH field is expected to be potentially measured in experiments by the femtosecond E-FISH [51], i.e., electric field-induced second harmonic generation method, that provides a resolution of sub-nano second in time and sub-millimeter in space for an electric field component in a given direction.

Finally, it is worth noting that we focus on the early stage of the plasma breakdown, where the plasma density is relatively low. With plasma density increasing for a longer discharge time, the electric field will significantly decay due to absorption and reflect within the discharge size of interest. The physics in high plasma density is beyond the scope of this work, and worth further investigation. In addition, the enhanced HH around ten times of the fundamental frequency in this work is investigated for tangential electric field. It is worth noting that vacuum multipactor discharge under oblique incident electric field was investigated in [15], and extra physics may be found in the presence of normal component of the incident rf electric field. In the future work, HH phenomenon will be further explored under oblique incident electric fields. The background gas is treated as static in order to consider more general cases, which can also be applicable to discharges with background gas. The desorption/outgassing process [52, 53] on the dielectric surface, that happens on a slower time scale due to pressure gradient-driven thermal diffusion is neglected in the current work, and it is worth further investigation on the effect of gas desorption in the future.

Acknowledgments

Fruitful discussions with Professor Hae June Lee of Pusan National University on the stream–plasma instabilities are highly appreciated. We also thank Professor Michael A Lieberman and Dr Emi Kawamura of University of California at Berkeley and Professor Jon Gudmundsson of University of Iceland for discussions in strictly benchmarking our PIC code with the well-established xpdp1 in a wide range of pressures. Discussions with Jinyu Yang from University of Notre Dame on possible measurement of electric field via E-FISH is highly appreciated. This work was supported by the Air Force of Scientific Research (AFOSR) MURI Grant Nos. FA9550-18-1-0062 and FA9550-21-1-0367 and NSF-DOE Partnership Grant for DE-SC0022078. YF acknowledges the support from the Tsinghua University Initiative Scientific Research Program and the State Key Laboratory of Power System and Generation Equipment (Project No. SKLD21M06).

Data availability statement

The data that support the findings of this study are available upon reasonable request from the authors.

Appendix. Dispersion relationship of stream–plasma interaction

In this appendix, we would show more detail on modelling the interaction between the secondary electron stream and plasma in collisional regime, and give the resulting dispersion relationship, which describes the oscillation frequency, growth rate of the amplitude of HH oscillation and wavenumber charactering the observed longitudinal oscillations in time and space [29]. In reference [47], a classical dispersion relationship for two-stream instabilities was given in absence of both electron–neutral collisions and pressure gradient term [54, 55]. These two effects are considered in our present work by extending the derivations in [47]. As measured in PIC simulation, the ionization electrons collectively move toward the window surface at a relatively low velocity, and surface secondary electrons are emitted and injected into the plasma as a cold stream. Here it is treated as a cold stream because the velocity distribution is close to a Dirac-δ function. We model these ionization electrons (labeled as 'ie') and secondary electrons (labeled as 'se') as two species of fluid flowing in opposite directions. The ions are nearly immobile during one rf period and treated as background, which will not affect the HH oscillations. The 'ie' has a velocity of $v_{\rm ie}$ and density of $n_{\rm ie}$, and the 'se' flows with a velocity of $v_{\rm se}$ and density of $n_{\rm se}$. Within the time scale of HH oscillations, the electron density slowly increases and is assumed unaffected by the ionization collisions. Thus, the dynamics of 'ie' can be described by the continuity equation,

$$\frac{\partial n_{\rm ie}}{\partial t}+\frac{\partial v_{\rm ie}n_{\rm ie}}{\partial x}=0 \tag{A.1}$$

and momentum balance equation

$$\frac{\partial v_{\rm ie}}{\partial t}+v_{\rm ie}\frac{\partial v_{\rm ie}}{\partial x}=-\frac{e}{m}E_x-\frac{\nabla p_{\rm ie}}{n_{\rm ie}}-\nu_m v_{\rm ie}, \tag{A.2}$$

where E_x is the space charge-induced normal electrostatic field, and $\nabla p_{\rm ie}=\partial(n_{\rm ie}k_{\rm B}T_{\rm iexxx})/\partial x$ is the x component of the pressure gradient, $k_{\rm B}$ is the Boltzmann constant, and $\nu_{\rm m}$ is the effective electron–neutral momentum transfer frequency of 'ie'. The normal longitudinal electrostatic field, $E_x=-\nabla_x\phi$, can be obtained through Poisson's equation

$$\nabla^2\phi=-\frac{\rho}{\epsilon_0} \tag{A.3}$$

with ρ the charge density. Let us define a general time-dependent physical quantity A to present the 'ie' fluid velocity and density, as well as the spatial potential, separately, and represented by two terms

$$A=A_0+\delta A \tag{A.4}$$

with A_0 a slowly varying zero order quantity following the fundamental frequency field, and a fast longitudinal oscillation term $\delta A=\tilde{A}\,{\rm e}^{{\rm j}(kx-\omega t)}$ at angular frequency ω and wavenumber k, with the unit complex number j. Thus, the growth and frequency of oscillations in time can be described by the imaginary and real part of ω, respectively. The oscillations are assumed to grow over time only, leading to a real number k. Using $n_{\rm ie}$, $v_{\rm ie}$ and ϕ to replace A, separately, and inserting them into equations (A.1) and (A.2), we obtain

$$\frac{\partial(n_{\rm ie0}+\delta n_{\rm ie})}{\partial t}+\frac{\partial(v_{\rm ie0}+\delta v_{\rm ie})(n_{\rm ie0}+\delta n_{\rm ie})}{\partial x}=0 \tag{A.5}$$

and

$$\begin{aligned}&\frac{\partial(v_{\rm ie0}+\delta v_{\rm ie})}{\partial t}+(v_{\rm ie0}+\delta v_{\rm ie})\frac{\partial(v_{\rm ie0}+\delta v_{\rm ie})}{\partial x}\\&=\frac{e}{m}\bigtriangledown(\phi_0+\delta\phi)-\frac{\bigtriangledown[(n_{\rm ie0}+\delta n_{\rm ie})k_{\rm B}T_{\rm iexx}]}{n_{\rm ie0}}-\nu_{\rm m}(v_{\rm ie0}+\delta v_{\rm ie})\end{aligned}. \tag{A.6}$$

Linearizing the above equations by neglecting the second order terms, and replacing the operators, $\partial/\partial t$ and $\partial/\partial x$ by $-{\rm j}\omega t$ and ${\rm j}kx$, respectively, we have

$$-{\rm j}\omega\tilde{n}_{\rm ie}+{\rm j}k(\tilde{v}_{\rm ie}n_{\rm ie0}+\tilde{n}_{\rm ie}v_{\rm ie0})=0 \tag{A.7}$$

and

$$-{\rm j}\omega\tilde{v}_{\rm ie}+{\rm j}k\tilde{v}_{\rm ie}v_{\rm ie0}={\rm j}k\frac{e}{m}\tilde{\phi}-{\rm j}k\frac{\tilde{n}_{\rm ie}k_{\rm B}T_{\rm iexx}}{n_{\rm ie0}}-\nu_{\rm m}\tilde{v}_{\rm ie}. \tag{A.8}$$

Combining (A.7) and (A.8), $\tilde{n}_{\rm ie}$ can be expressed as a function of $\tilde{\phi}$,

$$\tilde{n}_{\rm ie}=\frac{ke\tilde{\phi}/m}{\frac{(-\omega+kv_{\rm ie0}-{\rm j}\nu_{\rm m})(\omega-kv_{\rm ie0})}{kn_{\rm ie0}}+\frac{kk_{\rm B}T_{\rm iexx}}{n_{\rm ie0}m}}. \tag{A.9}$$

Similarly, the group of secondary electrons with positive fluid velocity are treated as a cold stream, and we have

$$\tilde{n}_{\rm se}=\frac{ke\tilde{\phi}/m}{(-\omega+kv_{\rm se0})(\omega-kv_{\rm se0})/kn_{\rm se0}} \tag{A.10}$$

after omitting the pressure gradient (thermal effect) and collisional term. Substituting (A.9) and (A.10) into Poisson's equation (A.3), ultimately, the dispersion relationship describing the frequency and growth rate of oscillation and the wavenumber in collisional regime is obtained [29]

$$\begin{aligned}1=&\frac{\omega_{\rm ie0}^2}{(\omega-kv_{\rm ie0}+{\rm j}\nu_m)(\omega-kv_{\rm ie0})+k^2k_{\rm B}T_{\rm iexx}/m}\\&+\frac{\omega_{\rm se0}^2}{(\omega-kv_{\rm se0})(\omega-kv_{\rm se0})}\end{aligned} \tag{A.11}$$

with $\omega_{\rm ie0,se0}^2=e^2n_{\rm ie0,se0}/m\epsilon_0$.

Note that equation (A.11) is a highly nonlinear equation in the complex domain, which is not straightforward to be solved. Here, we rewrite it in a polynomial format:

$$1=\frac{1}{(\eta+\alpha_{\rm ie}+{\rm j}\beta_{\rm ie})(\eta+\alpha_{\rm ie})+\xi_{\rm ie}}+\frac{1}{(\gamma\eta+\alpha_{\rm se})(\gamma\eta+\alpha_{\rm se})}, \tag{A.12}$$

where $\eta = \omega/\omega_{ie}$, $\gamma = \omega_{ie}/\omega_{se}, \alpha_{ie} = -kv_{ie0}/\omega_{ie}$, $\beta_{ie} = \nu_m/\omega_{ie}$, $\xi_{ie} = k^2 k_B T_{iexx}/m\omega_{ie}^2$, and $\alpha_{se} = -kv_{se0}/\omega_{se}$. Further simplifying gives

$$p_4\eta^4 + p_3\eta^3 + p_2\eta^2 + p_1\eta + p_0 = 0, \tag{A.13}$$

where $p_4 = a_1a_2, p_3 = a_1b_2 + b_1a_2, p_2 = c_1a_2 + c_2a_1 + b_1b_2 - a_1 - a_2$, $p_1 = c_1b_2 + c_2b_1 - b_1 - b_2, p_0 = c_1c_2 - c_1 - c_2$ with $a_1 = 1$, $b_1 = 2(\alpha_{ie} + j\beta_{ie})$, $c_1 = \alpha_{ie}^2 + j\beta_{ie}\alpha_{ie} + \xi_{ie}$, $a_2 = \gamma^2$, $b_2 = 2\gamma(\alpha_{se})$, $c_2 = \alpha_{se}^2$. Solving equation (A.13) gives four pairs of roots including the real part and complex part of η. Omitting three pairs of roots beyond the range of interest, we would obtain the final solution representing the real physical mode.

ORCID iDs

De-Qi Wen https://orcid.org/0000-0002-2662-9777
Peng Zhang https://orcid.org/0000-0003-0606-6855
Janez Krek https://orcid.org/0000-0002-0295-0232
Fu Yangyang https://orcid.org/0000-0001-9593-3177
John P Verboncoeur https://orcid.org/0000-0002-7078-3544

References

[1] Lieberman M and Lichtenberg A 2005 *Principles of Plasma Discharges and Materials Processing* 2nd edn (New York: Wiley)
[2] Kishek R A and Lau Y Y 1998 Multipactor discharge on a dielectric *Phys. Rev. Lett.* **80** 193
[3] Power J G, Gai W, Gold S H, Kinkead A K, Konecny R, Jing C, Liu W and Yusof Z 2004 *Phys. Rev. Lett.* **92** 164801
[4] Hidaka Y, Choi E, Mastovsky I, Shapiro M, Sirigiri J and Temkin R 2008 *Phys. Rev. Lett.* **100** 035003
[5] Schaub S C, Shapiro M A and Temkin R J 2019 *Phys. Rev. Lett.* **123** 175001
[6] Kishek R A, Lau Y Y, Ang L K, Valfells A and Gilgenbach R M 1998 Multipactor discharge on metals and dielectrics: historical review and recent theories *Phys. Plasmas* **5** 2120–6
[7] Valfells A, Ang L K, Lau Y Y and Gilgenbach R M 2000 *Phys. Plasmas* **7** 750–7
[8] Chang C, Zhu M, Verboncoeur J, Li S, Xie J, Yan K, Luo T and Zhu X 2014 *Appl. Phys. Lett.* **104** 253504
[9] Wang H, Liu D, Liu L, Xie M and Meng L 2018 *Plasma Sources Sci. Technol.* **27** 125006
[10] Wang H, Liu D, Liu L and Meng L 2020 *Plasma Sources Sci. Technol.* **29** 037001
[11] Wong P Y, Lau Y Y, Zhang P, Jordan N, Gilgenbach R M and Verboncoeur J 2019 *Phys. Plasmas* **26** 112114
[12] Iqbal A, Wong P Y, Wen D-Q, Lin S, Verboncoeur J and Zhang P 2020 *Phys. Rev.* E **102** 043201
[13] Valfells A, Verboncoeur J P and Lau Y Y 2000 *IEEE Trans. Plasma Sci.* **28** 529–36
[14] Kim H C and Verboncoeur J P 2005 *Phys. Plasmas* **12** 123504
[15] Wen D-Q, Zhang P, Fu Y, Krek J and Verboncoeur J P 2019 *Phys. Plasmas* **26** 123509
[16] Wen D-Q, Iqbal A, Zhang P and Verboncoeur J P 2019 *Phys. Plasmas* **26** 093503
[17] Michizono S, Saito Y, Yamaguchi S, Anami S, Matuda N and Kinbara A 1993 *IEEE Trans. Electr. Insul.* **28** 692
[18] Neuber A A, Edmiston G F, Krile J T, Krompholz H, Dickens J C and Kristiansen M 2007 *IEEE Trans. Magn.* **43** 496
[19] Foster J, Thomas M and Neuber A A 2009 *J. Appl. Phys.* **106** 063310
[20] Chang C, Liu G Z, Tang C X, Chen C H, Shao H and Huang W H 2010 *Appl. Phys. Lett.* **96** 111502
[21] Zhang P, Lau Y Y, Franzi M and Gilgenbach R M 2011 Multipactor susceptibility on a dielectric with a bias dc electric field and a background gas *Phys. Plasmas* **18** 053508
[22] Kim H C and Verboncoeur J P 2006 *Phys. Plasmas* **13** 123506
[23] Nam S K and Verboncoeur J P 2009 *Phys. Rev. Lett.* **103** 055004
[24] Boeuf J-P, Chaudhury B and Zhu G Q 2010 *Phys. Rev. Lett.* **104** 015002
[25] Zhu G Q, Boeuf J-P and Chaudhury B 2011 *Plasma Sources Sci. Technol.* **20** 035007
[26] Zhang J, Luo W, Jiang M, Wang H, Li Y and Liu C 2020 *Plasma Sources Sci. Technol.* **29** 025013
[27] Lau Y Y, Verboncoeur J P and Kim H C 2006 *Appl. Phys. Lett.* **89** 261501
[28] Wen D-Q, Zhang P, Krek J, Fu Y and Verboncoeur J P 2021 *Appl. Phys. Lett.* **119** 264102
[29] Wen D-Q, Zhang P, Krek J, Fu Y and Verboncoeur J P 2022 *Phys. Rev. Lett.* **129** 045001
[30] Kodheli O *et al* 2021 *IEEE Commun. Surv. Tutorials* **23** 70–109
[31] Iqbal A, Wong P Y, Verboncoeur J P and Zhang P 2020 *IEEE Trans. Plasma Sci.* **48** 1950–8
[32] Kishek R and Lau Y Y 1995 *Phys. Rev. Lett.* **75** 1218
[33] Vaughan R M 1993 *IEEE Trans. Electron Devices* **40** 830
[34] Gudmundsson J T, Kawamura E and Lieberman M A 2013 *Plasma Sources Sci. Technol.* **22** 035011
[35] Wen D-Q, Krek J, Gudmundsson J T, Kawamura E, Lieberman M A and Verboncoeur J P 2021 *Plasma Sources Sci. Technol.* **30** 105009
[36] Vahedi V, Birdsall C K, Lieberman M A, DiPeso G and Ronhlien T D 1993 *Plasma Sources Sci. Technol.* **2** 273–8
[37] Iqbal A, Verboncoeur J and Zhang P 2018 Multipactor susceptibility on a dielectric with two carrier frequencies *Phys. Plasmas* **25** 043501
[38] Biagi S 2004 *Cross Sections Extracted from Program MAGBOLTZ, Version 7.1* http://lxcat.net/Biagi-v7.1
[39] Hayashi M 2021 A data set of electron–Ar cross sections with 25 excited states http://lxcat.net/hayashi
[40] Eggarter E 1975 *J. Chem. Phys.* **62** 833–47
[41] Krishnakumar E and Srivastava S K 1988 *J. Phys. B: At. Mol. Opt. Phys.* **21** 1055–82
[42] Vikor D, Minic M, Cadez I and Kurepa M 1989 *Fizika* **21** 345–54
[43] Phelps A V 1994 *J. Appl. Phys.* **76** 747–53
[44] Vahedi V and Surendra M 1995 *Comput. Phys. Commun.* **87** 179–98
[45] Gudmundsson J T and Lieberman M A 2011 *Phys. Rev. Lett.* **107** 045002
[46] Zhang Z, Sun Y, Cui W, Zhang H, Huang Y and Chang C 2019 *IEEE Trans. Electron Devices* **66** 4921–7

[47] Birdsall C and Langdon A 2004 *Plasma Physics via Computer Simulation* 2nd edn (Beograd: Institute of Physics)
[48] Lafleur T, Chabert P and Booth J P 2014 *Plasma Sources Sci. Technol.* **23** 035010
[49] Kawamura E, Lieberman M A and Lichtenberg A J 2014 *Phys. Plasmas* **21** 123505
[50] Vass M, Wilczek S, Lafleur T, Brinkmann R P, Donkó Z and Schulze J 2021 *Plasma Sources Sci. Technol.* **30** 065015
[51] Yang J, Barnat E V, Im S-k and Go D B 2022 *J. Phys. D: Appl. Phys.* **55** 225203
[52] Chang C, Liu G, Tang C, Chen C, Qiu S, Fang J and Hou Q 2008 *Phys. Plasmas* **15** 093508
[53] Aldan M T P 2015 Modeling and simulation of electrical breakdown in DC for dielectric-loaded systems with non-orthogonal boundaries including the effects of space-charge and gaseous collisions *PhD Thesis* University of California, Berkely
[54] Sydorenko D, Kaganovich I D, Ventzek P L G and Chen L 2016 *Phys. Plasmas* **23** 122119
[55] Kaganovich I D and Sydorenko D 2016 *Phys. Plasmas* **23** 112116